Vortex rings impinging on permeable boundaries

Authors: Mujal-Colilles, Anna[1]; Dalziel, Stuart B.[2]; Bateman, Allen[3]

Affiliation

1. Anna.mujal@upc.edu. Marine Engineering Laboratory. Barcelona Tech-UPC, Barcelona, SPAIN

2. Department of Applied Mathematics and Theoretical Physics. Cambridge University, UK.

3. Sediment Transport Research Group. Barcelona Tech- UPC, Barcelona Spain.

Abstract

Experiments with vortex rings impinging permeable and solid boundaries are presented in order to investigate the influence of permeability. Utilizing Particle Image Velocimetry (PIV), we compared the behaviour of a vortex ring impinging four different reticulated foams (with permeability $k \sim 26 - 85 \times 10^{-8} \text{m}^2$) and a solid boundary. Results show how permeability affects the stretching phenomena of the vortex ring and the formation and evolution of the secondary vortex ring with opposite sign. Moreover, permeability also affects the macroscopic no-slip boundary condition found on the solid boundary, turning it into an apparent slip boundary condition for the most permeable boundary. The apparent slip-boundary condition and the flux exchange between the ambient fluid and the foam are jointly responsible for both the modified formation of the secondary vortex and changes on the vortex ring diameter increase.

1   Introduction

Vortex rings form spontaneously in many unsteady processes found in nature. Volcanic eruptions, swimming squid, starting jets and some dolphin games all involve structures taking the form of vortex rings. Some industrial processes use the impingement of a vortex ring onto a solid surface to dislodge the particles that can be trapped in it (see [1]), and vortex rings are a serious issue when landing a helicopter (e.g. [2], [3]).

The first analysis of a vortex ring structure was described by Lord Kelvin [4] for vortex rings with a very thin core compared to the ring diameter. At the opposite limit, Hill [5] detailed the characteristics of a vortex ring with the core diameter equal to the radius of a vortex ring, a structure now known as the Hill's spherical vortex. Batchelor [6] described vortex rings as a single circular line vortex for inviscid fluids where the core was infinitesimally small and the propagation velocity was infinite. Subsequently, Norbury [7] proposed a theoretical expression for vortex rings with a thin size of the core and a finite velocity of propagation and extended this to the entire range of vortex rings with different core sizes. Maxworthy [8] carried out a series of experiments with different vortex ring formation characteristics to study its influence on the velocity of propagation, the core size and the existence of instabilities; his studies revealed the existence of entrainment causing vortex deceleration.

A model for the canonical case of a vortex ring impinging a perpendicular solid wall was proposed by Saffman [9], using the mirroring of a vortex pair moving towards a symmetric vortex pair (with the plane of symmetry perpendicular to the direction of the motion). Cerra et al. [10] and Walker et al. [11] pioneered the experimental study of the vortex ring impacting on a solid boundary, with Orlandy and Verizcco [12] and Swearingen et al. [13] undertaking some of the earliest simulations. They all found a stretching of the core when approaching the wall, an increase in the diameter of the vortex ring, and the existence of a rebound of the core parallel to the formation of a secondary vortex with opposite sign [14].

More recently, attention has turned to the possibility of resuspension due to a vortex ring impacting a bed of particles (e.g. [1], [15], [16], [17] and [18]). Of particular interest here is the suggestion by Bethke and Dalziel [19] that the permeability/porosity of the sediment bed may influence the dynamics of the interaction.

In previous studies, the interaction of vortex rings with porous boundaries has been related mainly to thin permeable grids with different porosity and wire diameter. Adhikari and Lim [20] and Naaktgeboren et al. [21] compared the impact of a thin porous grid on the vortex ring propagation with the interaction with a solid wall, varying mainly the Reynolds number and the grid porosity (defined as the ratio between the void spaces and the total area of the grid). They found that porosity influenced the increase of the vortex ring diameter: rings impinging higher porosity grids did not increase their diameter while

60   approaching the grid. Moreover, the existence of the secondary vortex cores disappeared
61   and the vortex ring was transmitted through the grids. Hryunk et al. [22] showed how the
62   scales of the grid also influenced the vortex/grid interaction. In particular, they studied
63   constant porosity grids with variable wire diameter using constant Reynolds number
64   vortex rings, and showed how the propagation of the ring beyond the grid was influenced
65   by the length scales of the grid.

66   The work presented herein focuses on the interaction of vortex rings with thick permeable
67   boundaries, relative to the core diameter, overlying impermeable base. This research aims
68   to explore the influence of such boundaries on the vortex ring propagation.

69   This paper is organized as follows. The experimental methods and basic configuration
70   are introduced in section 2, while section 3 presents the main experimental results. These
71   results are discussed in section 4 and finally, conclusions are presented in section 5.

72   ## 2   Materials and Methods
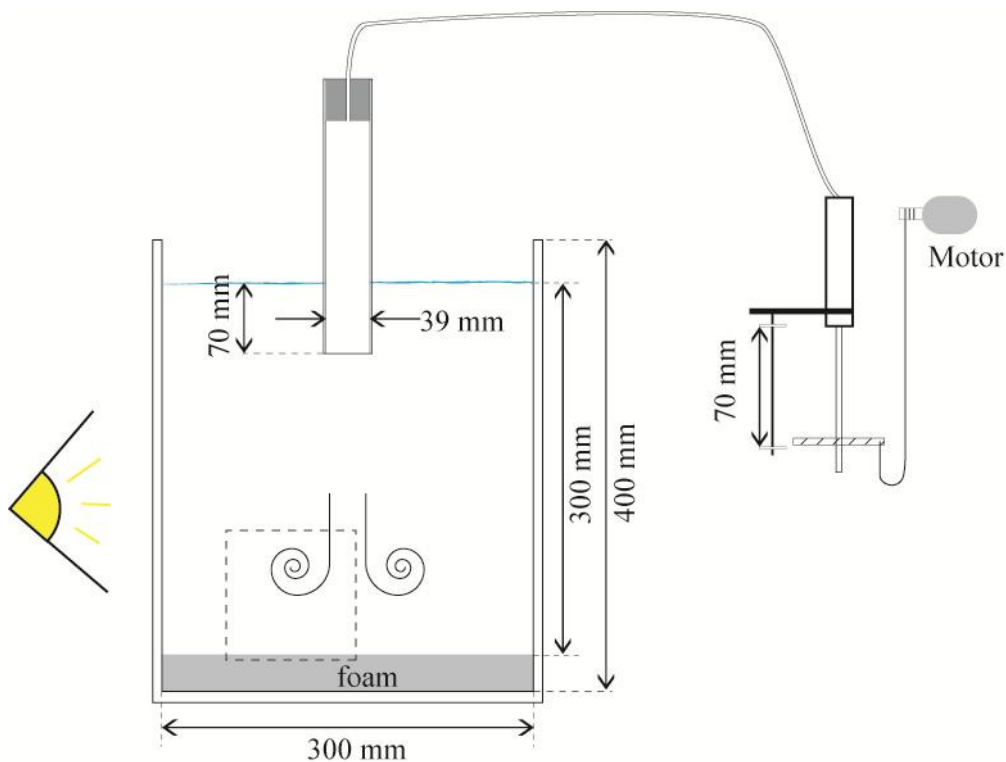
73

74   **Figure 1. Sketch of the experiment setup. Dashed square marks the field of view recorded.**

75   The experiments were carried out using a 36 litre acrylic tank, essentially the same as that
76   described by [17] and [19]. The tank has a square base (300×300 mm), and a 400 mm

77 height. The front face was left completely transparent, while the bottom and two lateral

78 faces were covered on the inside with matt black plastic film to avoid the influence of

79 ambient light; the third vertical face was covered with the same film except for a narrow

80 vertical slot to allow illumination by a thin light sheet (see Figure 1). The lower boundary

81 was either solid (using the base of the tank), or porous (using blocks of reticulated

82 polyether foam cut to fit within the tank; see below). In either case, the tank was always

83 filled to a depth of 300 mm above the top of the porous/permeable boundary: this is the

84 bottom of the tank in the solid boundary experiments and the top of the porous layer in

85 permeable boundary cases. The tank was filled with a column of salty water ($\rho = 1020$

86 kg/m^3) to ensure the particles used for measuring the velocity field were neutrally

87 buoyant.

88 The vortex ring was created in the same manner as used by [17] and [19]. In particular, a

89 PVC tube of internal diameter D_t = 39 mm was submerged to a depth of 70 mm beneath

90 the surface of the water. A slug of water was driven out the end of the tube by introducing

91 air from a bicycle 'track pump'. This pump, with internal diameter D_s = 29 mm, was

92 actuated by an electric motor connected to its handle via a piece of nylon cord wound

93 onto a capstan. For the experiments presented here, the stroke length for the pump was

94 set to L_s = 70 mm and the stroke time held constant at T_s = 141.9±1.1 ms. The formation

95 number for the vortex rings,

$$N = \frac{L}{D_t} = \frac{L_s D_s^2}{D_t^3}, \tag{1}$$

97 is around one. Here, L is the length of the slug of water expelled from the tube. The

98 Reynolds number, $Re = V_r D_t / v$ (V_r is the vertical propagation velocity of the ring before

99 the deceleration starts) is kept constant in all the experiments with a value around $5 \times$

100 10^3; some other researchers prefer to use the Reynolds number based on the circulation,

101 $Re_\Gamma = \Gamma / v$ (being Γ the circulation), which in our case is a value in the order of 2×10^3.

102 This value lies within the laminar regime and is comparable to the lower circulation

103 Reynolds number cases of the experiments performed by other authors (i.e. [17], [18] and

104 [19]), and is within the larger scenarios performed by other research articles (i.e. [11],

105 [12] and [13]).

106 Table 1: Characteristics of the foams used. Ppi Range and height (*h*) values are given by the
107 manufacturers. Vertical hydraulic conductivity (*K$_z$*) values are obtained experimentally and vertical

| Foam name	*Ppi Range*	D_p *(mm)*	*h (mm)*	K_z *(m/s)*	k_z *(10^{-8} m^2)*
k26	60	0.5	25	0.24	26
k51	30	1	25	0.48	51
k70	20	2	25	0.65	70
k85	10	3	50	0.79	85

110 Table 1 describes the main characteristics of the four different reticulated polyether foams
111 used to form the porous boundary. Each had an internal structure that was geometrically
112 similar but differed in scale (pore diameter), see Figure 2.The vertical permeability
113 component of the permeability tensor of each foam,

$$k = K\frac{\nu}{g}, \tag{2}$$

115 was determined by ensemble averaging the results obtained from 20 different Darcy's
116 tests (UNE-103403-99) for each foam with an estimate error of $\pm 2.5 \times 10^{-8}$ m² for k_z.
117 This data is given in Table 1. For convenience, we identify the foam blocks based on the
118 permeability values shown in Table 1. Foam blocks k26, k51 and k70 all had a thickness
119 of $h = 25$ mm, while k85, the coarsest (most permeable) foam, was thicker with $h = 50$
120 mm. We observed a weak anisotropy in the foams but calculations under the assumption
121 of Darcy's flow showed the anisotropy had negligible impact on the flow. In all cases, we
122 define our coordinate system so that $z = 0$ is the top of the block of foam. Before each
123 experiment, care was taken to ensure that no air bubbles were caught in the foam (a small
124 quantity of wetting agent was used to assist this process and the foam blocks were kept
125 submerged between experiments).
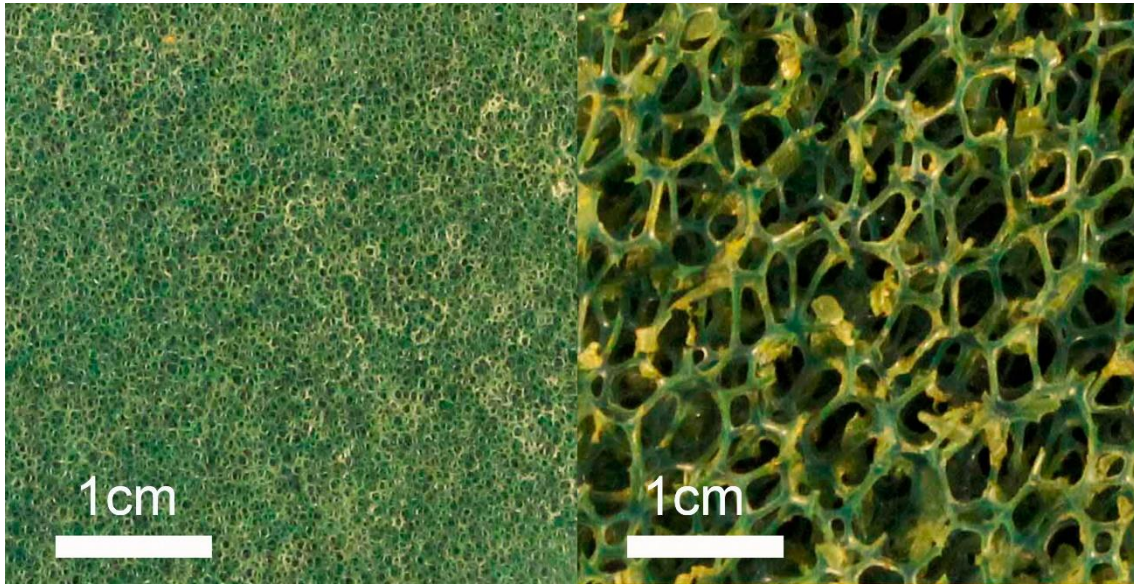
Figure 2. Left: photo of the k26 foam. Right: photo of the k85 foam.

In addition to the four porous foams, we studied the impact of the ring on a solid boundary, k0. We could treat this data as either the limit of zero permeability (placing our coordinate origin $z = 0$ at the solid boundary) or the infinite permeability limit for a foam block of thickness h by considering the bottom of the tank as $z = -h$, k∞. The tank bottom was smooth. However its classification with the porous foams was complicated by the existence of the flux of fluid and the horizontal momentum across the nominal upper surface. Therefore in the present experiments we are unable to detect any influence of the boundary roughness.

The experiments presented here were illuminated by a light sheet from a 300 W xenon arc lamp fitted with a parabolic dichroic reflector. Nearly collimated light from the lamp passed between adjustable aluminium strips on the side of the tank to generate a sheet with a thickness of about 3 mm. The experiments were recorded using a high-speed 1 MPixel camera (Photron SA1.1) at 1000 frames per second. The camera was fitted with a 60mm AF micro NIKKOR lens with a f = 2.8 aperture. For some experiments, the field of view covered the whole diameter of the vortex ring, although for others, only one side of the ring was visualised in order to improve spatial resolution. For such experiments, the camera was located around 360 mm from the light sheet.

Our main experimental results were obtained using PIV on one half of the vortex ring (see sketch in Figure 1). As discussed in the next section, our field of view was sufficient to ensure it captured the majority of the interaction between the ring and the porous

148 boundary. We used Pliolite VTAC particles with nominal diameter between 70 and 110

149 μm and specific gravity around 1.02. These particles were rendered neutrally buoyant

150 through the addition of 35 g/l of salt (NaCl) to the water in the tank. The PIV analysis

151 was performed using the software DigiFlow [23] with interrogation regions 21×21 px^2 at

152 a spacing of 15 pixels giving an effective spatial resolution of 1.4 mm. A cubic spline

153 algorithm was used to interpolate between PIV results and acquire feasible results at every

154 pixel, as part of an image distortion scheme used in the pattern matching process.

155 We also present experiments visualised using a precipitation technique driven by the

156 electrolysis of electrical solder. A thin solder-covered ('tinned') copper foil was stuck to

157 the inside of the open end of the PVC tube. A brief pulse of current was passed through

158 this foil (attached to the positive side of a DC power supply) to produce a cloud of white

159 precipitate just prior to ejecting the vortex ring (hydrogen bubbles were produced at the

160 second electrode that was placed in a remote corner of the tank). This precipitate was

161 largely confined to the boundary layer exiting the tube and so was wrapped up into the

162 core of the vortex ring. Illuminating the whole domain allowed us to confirm that the

163 rings remained essentially axisymmetric throughout their interaction with the porous

164 boundary.

3   Experimental Results

166 We begin with some qualitative visualisations of the interaction between the vortex ring

167 and the various boundaries using the precipitation technique described in the previous

168 section. Using a sheet of light passing through the axis of the ring, Figure 3a shows the

169 interaction with a solid boundary, k0, while Figure 3b shows the interaction with the k85

170 (coarsest) foam. Both images are for the same time after generating the ring. In the

171 absence of the boundaries, the two rings would be indistinguishable and their cores would

172 be located at $z = 0$, the position of the boundary. However, Figure 3a illustrates clearly

173 the radial stretching of the ring as it begins to interact with its 'image' in the solid

174 boundary. In contrast, the concept of an image vortex ring to impose no normal flow

175 across the boundary is not applicable to the porous boundary in Figure 3b. Although there

176 has been some stretching and deceleration of the ring, this is nowhere near as pronounced

177 as was seen for the solid boundary, and consequently the core diameter remains large. As

178 we shall see, this behaviour is typical for the permeable interactions. The ring's

179 interaction with the solid boundary also deposits secondary vorticity of the opposite sign
180 on the wall as a result of the no-slip boundary condition. The presence of a small amount
181 of precipitate outside the core of the ring makes this visible in Figure 3a, where separation
182 of this secondary vorticity is leading to the emergence of a coherent secondary vortex that
183 is beginning to wrap some of the precipitate around it. While this is happening around the
184 entire body of the vortex ring, the illumination makes this clearer in the vicinity of the
185 left-hand core in the Figure 3a. In contrast, there is no clear evidence from Figure 3b of
186 such a structure existing in the interaction with the porous k85 boundary.
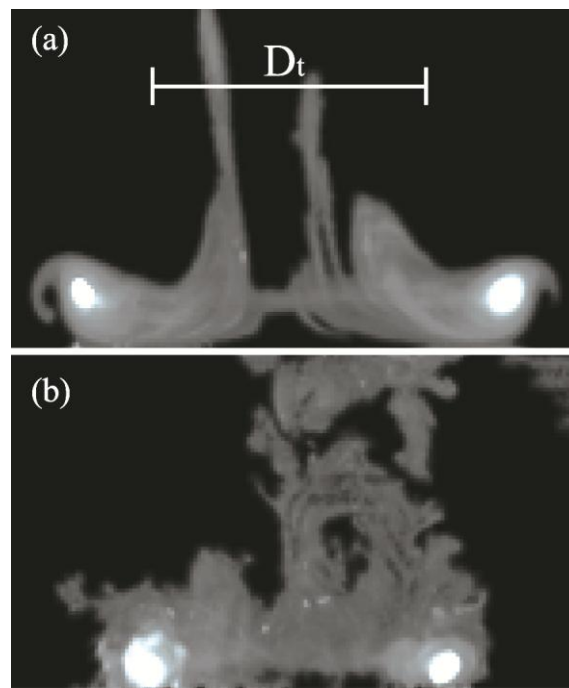
187

188 **Figure 3. Comparison of the vortex ring interaction between solid boundary –upper- and a coarse**
189 **foam –lower- visualized using the electrolytic precipitation of tin chloride.**

190 Figure 4 offers the same form of visualisation across our entire range of porous and solid
191 boundaries. These images are arranged so that the boundary permeability increases from
192 left to right. The upper row of the figure (Figure 4a-e) shows the similarity of the rings at
193 a height $z = D_t$ above the wall (henceforth we label this height as our time origin $t = 0$).
194 The cores of the rings are at the same height and of the same size; small variations in the
195 k0 case are due to imprecisions in the way the precipitate is introduced and henceforth
196 considered negligible not only in the k0 case but also in other cases. The images in the
197 lower row of Figure 4 (panels f to j) are from the same five experiments as the upper row

198 but show the position of the cores with $\tilde{t} = \dfrac{V_r}{D_t} t = 1.05$. Clearly, increasing the

199 permeability allows the rings to approach the boundary more closely while reducing the
200 stretching of the diameter of the ring. The precipitate outside the core may give the
201 appearance to have tilted vortex rings. However this effect is due to the Kelvin waves, or
202 azimuthal instabilities, meaning the slice through the ring may sample the core at different
203 phases producing this apparent inclination.
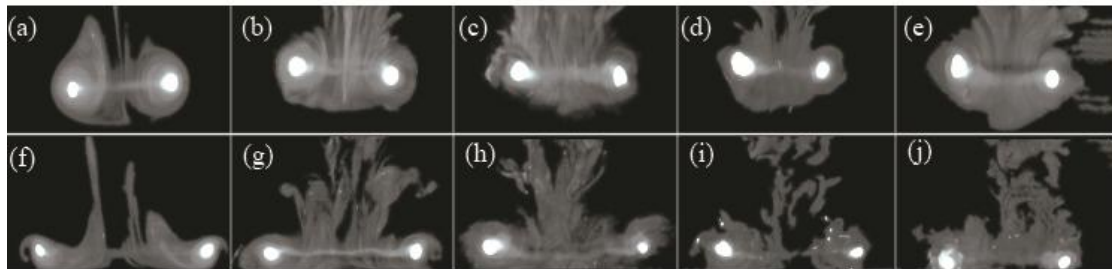
204

205 **Figure 4. Upper row $\tilde{t} = 0$; lower row $\tilde{t} = 1.05$. Column-wise, from left to right with increasing**
206 **permeability k0 (a,f), k26 (b,g), k51 (c,h), k70 (d,i), k85 (e,j)**
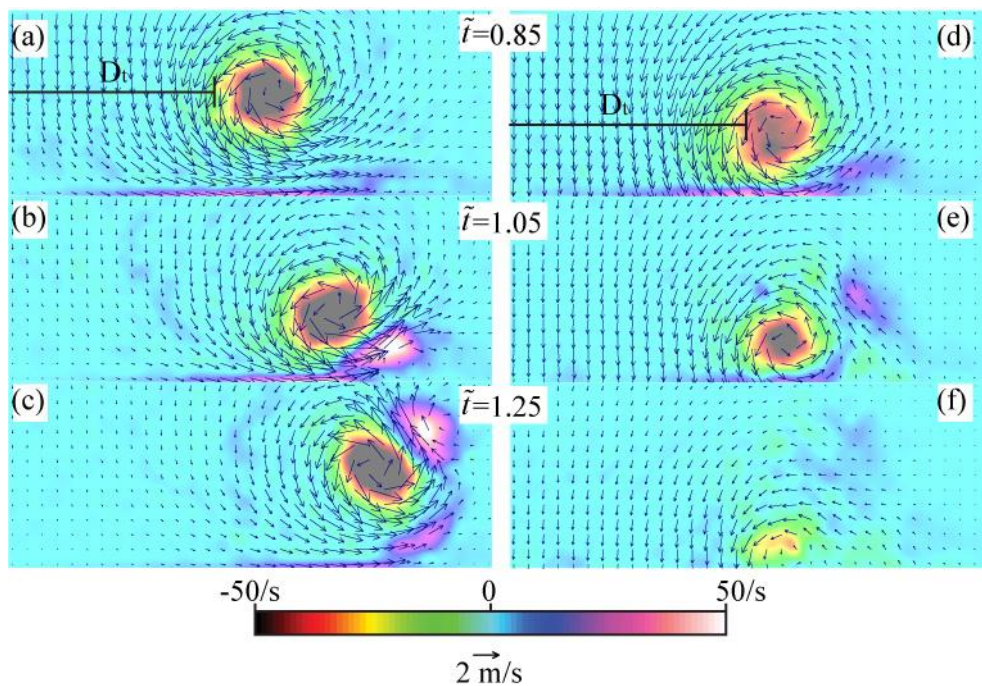
207

208 **Figure 5. PIV results of a vortex ring approaching two different boundaries. (a) to (c) solid**
209 **boundary (k0); (d) to (f) coarsest foam k85. Background variable: vorticity.**

210 The PIV experiments give more detail about the different behaviour when using porous
211 boundaries. Figure 5 shows velocity and vorticity fields at different dimensionless times
212 for the of k0 and k85 boundaries. Figure 5a-c shows the flow above the k0 solid boundary
213 (the symmetry axis of the vortex ring is located on the left-hand side of the field of view).
214 As seen by previous authors and noted above, the no-slip boundary condition has
215 generated secondary vorticity at the boundary that has begun to separate to form a

216   secondary vortex ring. This secondary vortex ring interacts with the primary ring to
217   further retard and temporarily reverse the primary ring's direction of vertical propagation.
218   Secondary vorticity continues to be generated at the boundary and is wrapped around the
219   primary ring as the stronger circulation in the primary ring sweeps the secondary ring out
220   and around it before compressing it back towards the axis. As discussed by others (e.g.
221   [8] and [24]), the compression of this secondary ring plays an important role in the
222   development of instabilities and the eventual break-up of the primary vortex ring.

223   Figure 5d-f shows how the coarsest foam (k85) fundamentally changes the nature of the
224   interaction. First, the k85 boundary lets the vortex ring get closer to the boundary and the
225   core begin to penetrate it. Second, the changes in diameter are not as significant when a
226   permeable boundary is used since the secondary vortex does not have the same intensity
227   as in the case of the solid boundary interaction. Finally, although secondary vorticity is
228   perceptible in Figure 5 (d) and (e), it is comparably weaker than the solid boundary case,
229   indicating it can also affect the relevance of the no slip boundary condition assumed in
230   the k0 scenario.

231   In Figure 6 we summarise the behaviour of the core of the primary vortex ring with the
232   ensemble of 10 PIV experiments for each of the different boundary permeabilities. In
233   particular, we use the vorticity criterion of Bethke and Dalziel [19] to locate the cores of
234   the vortex rings from the PIV measurements. The trajectory of the cores is shown in

235   Figure 6a. Here we plot $\tilde{Z} = \dfrac{Z}{D_t}$ against $\tilde{D} = \dfrac{2R}{D_t}$, where R is the distance from the

236   symmetry axis to the centre of the core and Z represents the vertical position of the centre
237   of the core. In the absence of a lower boundary, the trajectory would be a vertical line
238   with constant $\tilde{D}$. The solid line shows the behaviour of the core above the solid
239   boundary, the diameter increasing as the ring approaches the boundary. Note the
240   characteristic rebound of the core at $\tilde{D} \approx 1.7$. This is due to the coupling between the
241   primary ring and the secondary ring following separation of the boundary layer. Figure
242   6b and c show the same trajectory data plotted as a function of dimensionless time. For
243   the k0 boundary, the rebound is clearly visible after the ring's closest approach at $\tilde{t} \approx 1$
244   with $\tilde{z}$ increasing then $\tilde{D}$ decreasing from $\tilde{t} \approx 1.1$.
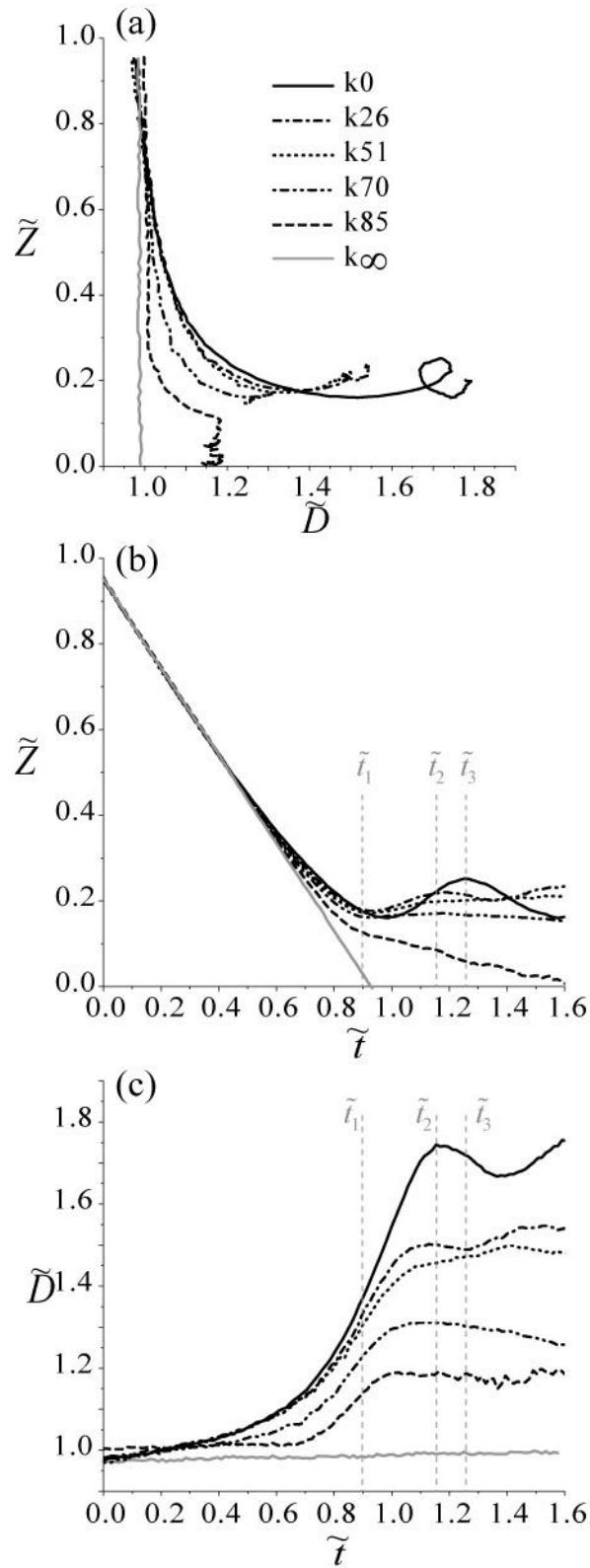
Figure 6. Comparison between boundary types with porous boundaries and solid boundary. a)Trajectory; b) vertical position evolution; c) diameter evolution.

As the permeability of the boundary increases (k26, dot-dashed lines), the diameter of the

ring grows slightly more slowly (Figure 6c) and the vertical velocity is reduced by less as

250   it approaches the boundary (Figure 6b) resulting in the trajectory lying below that of the

251   solid boundary until around $\tilde{t} = 1$, when the ring decelerates relatively quickly. A small

252   rebound is evident, although compared with the rebound from the solid boundary, the

253   rebound from k26 is smaller, earlier and at smaller radius. The trajectory above the k51

254   porous boundary (doted line) shows a slightly closer initial approach, more sudden and

255   slightly later deceleration, and a smaller spread than either the solid boundary or k26.

256   Although the approach of the core still changes direction (with the core moving away

257   from the boundary for $\tilde{t} > 1.0$), the diameter grows monotonically until much later.

258   The trajectories above the two coarsest foams (k70 dot-dot-dash lines and k85 long

259   dashes) continue the trend of not expanding as much as they approach the boundary. Their

260   approach velocity remains constant until about $\tilde{t} = 0.8$, after which they decelerate and

261   begin to grow in diameter more dramatically. There is some suggestion of a weak rebound

262   for the k70 boundary (although the distance from the boundary remains nearly constant

263   after $\tilde{t} \approx 1$, the diameter decreases slightly), but none for the most permeable boundary,

264   k85.

265   One open question is whether the thickness of the porous layer plays a role. It is obvious

266   that for the same vortex ring characteristics impacting a very thin porous layer, the

267   thickness will be important (comparing two foams with the same permeability), but it is

268   less clear whether our current porous layers are sufficiently thick for their thickness to be

269   unimportant, considering the tank has an impermeable base. To this end, the grey line in

270   Figure 6 replots the trajectory for the solid boundary case but offset downwards by $h = 50$

271   mm, the thickness of the most permeable (k85) foam. We can view this as representing

272   the limit of high permeability (with $h = 50$ mm layer thickness) where the porous

273   boundary ceases to play a significant role and only the solid boundary of the tank is

274   important. As can be seen in Figure 6a, the trajectory above this virtual k∞ foam by the

275   time the ring reaches $\tilde{z} = 0$ is nearly uninfluenced by the presence of a boundary and is

276   clearly different from the ring approaching the k85 foam.

277   According to Bethke and Dalziel [19], a vortex ring impinging a solid boundary begins

278   to stretch its diameter and decelerates at a height comparable to D_t. Figure 7(a) quantifies

279   the height at which the diameter of the ring starts increasing detected in Figure 6 (c), Z_t.

280   As seen in Figure 7(a), the vortex ring velocity remains constant for longer (to a lower

281   height) with more permeable boundaries. The extreme case is the k85 foam, when the

282 ring begins to decrease its downward propagationvelocity at a height equal to only 20%

283 of the diameter of the tube. On the other hand, Figure 7(b) plots the maximum rebound

284 height, Z_r, the maximum height of the primary core after $\tilde{t} > 1$ in Figure 6 (b). In the most

285 permeable case, k85, no rebound has been observed; we flag this by setting $Z_r = 0$.

286 Smaller permeabilities allow the vortex ring to slightly rebound, increasing Z_r up until

287 its maximum in the solid boundary case when it is around a quarter of the tube diameter,

288 D_t.
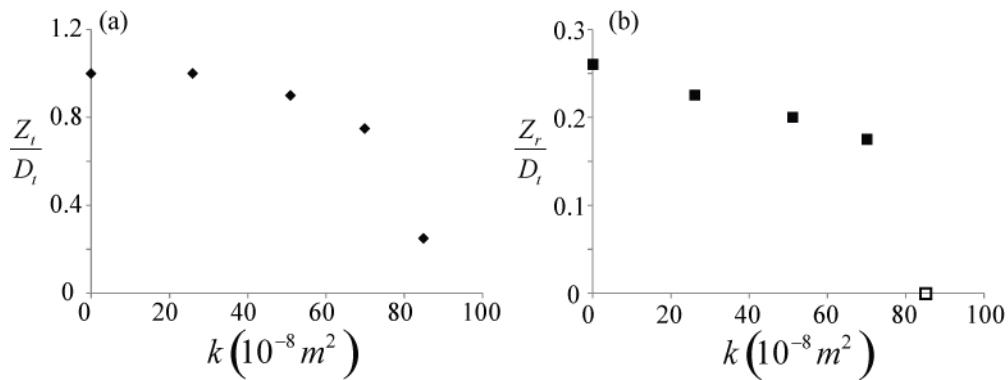

290 **Figure 7. Characteristic heights related to (a) the Z level at which the diameter of the initial ring**
291 **started stretching and (b) the maximum Z level reached during the primary vortex rebound.**

292 In order to reconcile the differences in behaviour of the vortex ring-boundary interaction,

293 we examine the velocity and vorticity fields for each case in Figure 8. We use three

294 specific times to compare all the different boundary types (see Figure 6 (b-c)). Although

295 the time for closest approach varies slightly with permeability (see Figure 6 (b-c)), we

296 shall take $\tilde{t}_1 \approx 0.90$ as representative of this. Similarly $\tilde{t}_2 \approx 1.15$ marks the time at which

297 the diameter is maximum for the k0 boundary, and $\tilde{t}_3 \approx 1.25$ is the time of the maximum

298 rebound height in the k0 boundary. Figure 8shows how the secondary vortex ring is

299 formed when the primary vortex ring interacts with a solid boundary. As has already been

300 described, the secondary ring is formed with the detachment of the boundary layer and

301 causes the decrease on the diameter of the primary vortex ring. From Figure 6(c), all

302 boundary types except k85 presented a decrease in diameter indicating the formation of

303 a secondary vortex ring. However, Figure 8 (e) shows evidence of weak secondary

304 vorticity in the k85 scenario, which may indicate why the primary ring in this case

305 increases its diameter up to a certain point when a secondary vortex ring is formed (around

306 $t \approx 1.0$).   As described before, the formation of this secondary ring is due to the

307   development of the boundary layer. Beavers and Joseph [25], Taylor [26] and Richardson

308   [27] suggest that the boundary layer penetrates into the porous media. Hence the weak

309   formation of the secondary vortex ring is clearly explained by increment in the extension

310   onto the foam material with porosity, affecting the boundary layer. This makes the

311   detachment of the boundary layer more difficult and consequently inhibits the formation

312   of this secondary vortex ring.

313
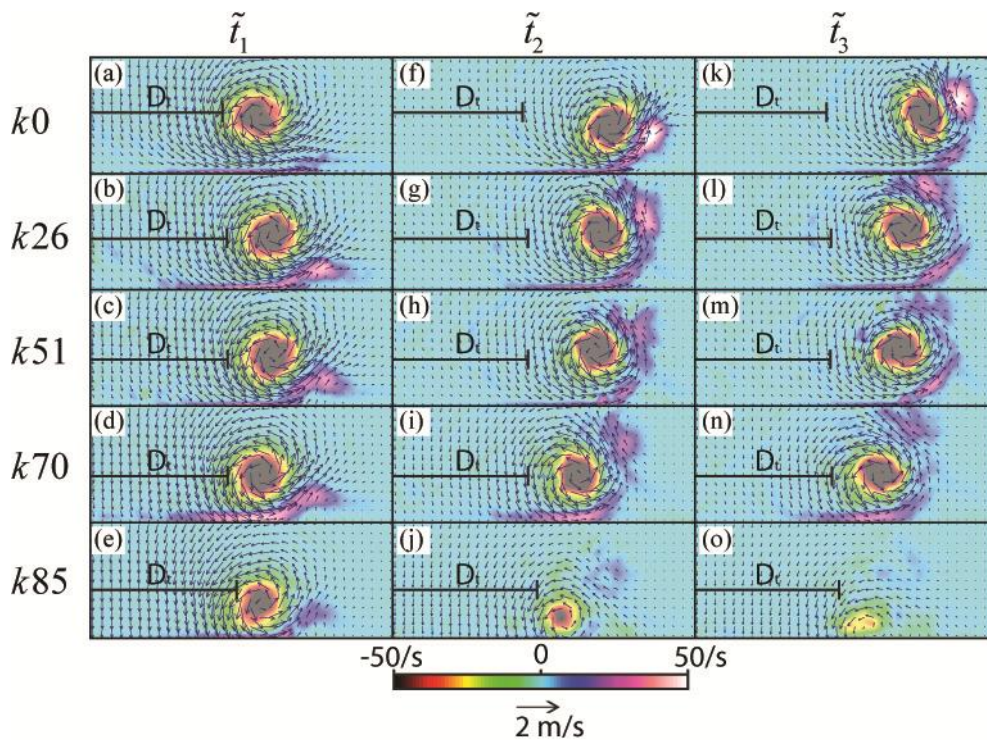
Figure 8. PIV results of half vortex ring at the time steps $\tilde{t}_1 \approx 0.90$, $\tilde{t}_2 \approx 1.15$, $\tilde{t}_3 \approx 1.25$ Background variable vorticity.

316   Figure 8 (f) is useful to see how the maximum diameter of the primary ring is reached

317   when the secondary vortex ring is at the same elevation as the primary vortex; Figure 8

318   (g-i) may confirm this since $\tilde{t}_2$ in the k26, k51 and k70 cases is soon after the maximum

319   diameter is attained, see Figure 6 (c), and the secondary vortex ring is located slightly

320   above the primary ring. The coarsest boundary, k85, does not show the complete

321   evolution of the secondary vorticity because the ring seems to penetrate into the foam.

322   Finally, Naaktgeboren et al. [21] described the existence of a third weak vortex ring

323   coming from the boundary layer which is observed in all foams except the k85 boundary

324   in Figure 8 (k-n).
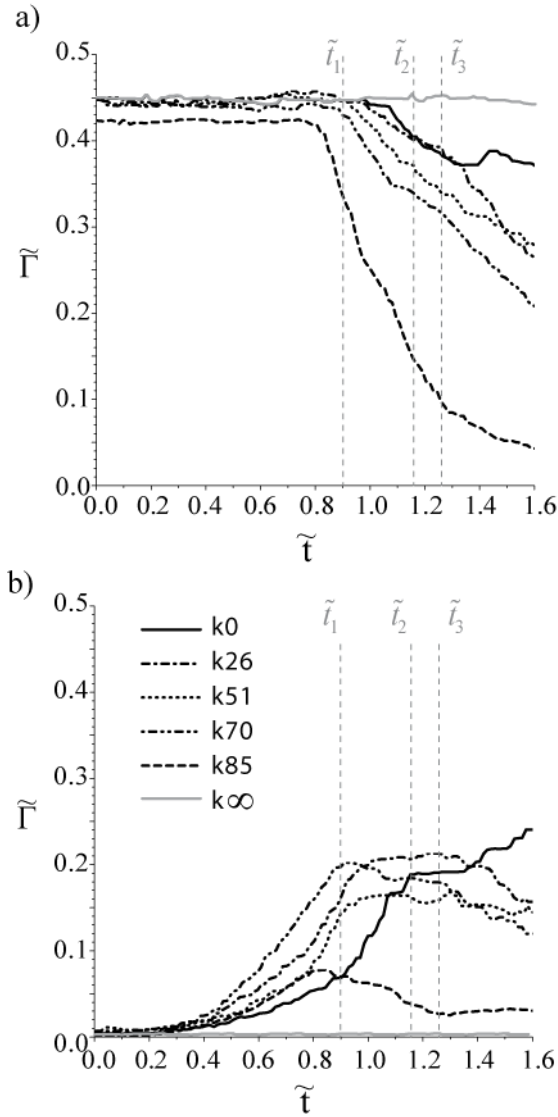
Figure 9. Evolution of the primary (a) and secondary (b) vorticity of the interaction of a vortex ring with different boundaries.

One variable of interest to emphasize the changes on the vortex ring interaction with different permeable boundaries is the evolution of the vortex ring circulation,

$$\Gamma = \int_{A_c} \omega \, dA \, , \tag{3}$$

where A_c is the area of the core. As detailed in Bethke [16], the definition of the core is somewhat controversial. Here, vorticity lying below 3% of the vorticity peak is considered noise and not used in the computation. Maximum vorticity (here negative) is found at the centre of the ring's core. Therefore primary circulation is computed as sum of the negative values within the defined threshold and the secondary circulation as the sum of positive values above the absolute value of the same threshold. This is accurate

337   for the primary vortex ring but may underestimate the circulation of secondary vortex

338   ring and boundary layer (where a larger fraction of the vorticity may be excluded from

339   the circulation calculation). However, this methodology is sufficient to reveal the

340   evolution of the circulation of the secondary vortex once the primary ring has started its

341   rebound and results are not sensitive to small changes in the threshold of the 3%. During

342   the vortex ring's approach to the wall, the secondary vorticity is generated in the boundary

343   layer; after the vortex ring has reached the wall, and at the early stages of the secondary

344   vortex formation, secondary vorticity from the boundary layer still represents the majority

345   of the secondary circulation. However, for $\tilde{t} > 1$, the secondary vortex has formed

346   through separation of the boundary layer and this secondary vortex represents the

347   dominant contribution to the secondary circulation.

348   Figure 9 plots the measurements of the non-dimensional circulation, $\tilde{\Gamma} = \dfrac{|\tilde{\Gamma}|}{(V_r D_t)}$, for

349   both the primary and secondary vorticity. The lower values of $\widetilde{\Gamma}$ in the k85 case of

350   primary circulation (Figure 9a) are mainly due to small errors accumulated on the

351   computation of the vertical velocity propagation of the ring before the beginning of the

352   deceleration, V_r. When the ring is impinging a solid boundary, secondary vorticity

353   appears due to the viscosity and the no slip boundary condition. Hence secondary

354   circulation starts increasing while the primary vortex ring approaches the wall because

355   the boundary layer at the wall starts developing; this is why the secondary circulation

356   starts increasing before the decrease in primary circulation. Primary circulation of the ring

357   is preserved during the initial stretching. However, when the ring is closer to the wall

358   ($\tilde{t} = \tilde{t}_1$), both the primary and secondary vorticity interact through molecular viscosity.

359   From this time on, primary circulation decreases while the secondary ring is being formed

360   by the detachment of the secondary vorticity present in the boundary layer. In the k0

361   scenario, circulation of the secondary vorticity has its peak coinciding with the point

362   where ring reaches its maximum diameter. After $\tilde{t}_1$, the primary circulation decrease is

363   faster for higher permeable boundaries, indicating that the interaction between the

364   primary and secondary vortex ring is generating more loses.

365   Figure 9b does not show a clear pattern of relationship between the secondary circulation

366   and permeability. This is caused by the strong influence of the interface level $\tilde{z} = 0$ on

367   the curves, mainly due to the light reflection contaminating the results. Around $\tilde{t}_1$ we can

368 distinguish two different behaviours: i) for the solid boundary case, k0, secondary
369 circulation increases faster after $\tilde{t}_1$, indicating that the boundary layer keeps forming at
370 the interface; ii) for all the permeable boundaries, secondary circulation peaks and either
371 keeps constant for the lower permeable cases, k26 and k51, or decreases for the larger
372 permeable cases, k70 and k85. Therefore, the boundary layer at the interface does not
373 grow as it does for the solid boundary case affecting the secondary vortex ring formation
374 and life: secondary vortex ring is weaker as the permeability increases, as shown in Figure
375 8. Finally, Figure 9 (b) reflects the existence of secondary vorticity in the coarsest
376 permeable boundary, k85, which can be related to the formation of the secondary vortex
377 ring as was detected in Figure 8e.

378 Figure 10 shows the vertical (left panel) and the horizontal (right panel) dimensionless
379 velocity profiles ($\tilde{v} = v/V_r$) measured 1 mm above the permeable or solid boundary. The
380 radius has been made dimensionless by $\widetilde{R} = R/D_t$. The marks represent the radial position
381 of the core at each time, and the time profiles coincide with the frames plotted in Figure
382 8. In absolute terms, vertical velocities close to the boundary increase with permeability
383 whereas horizontal velocities decrease. Larger horizontal and vertical velocities are
384 reached at $\tilde{t}_1$, except for the k0 and the k85 cases, compared to other instants in the figure.
385 In the k0 scenario, this is because the ring has not reached its closest approach to the
386 boundary, whereas in the most permeable k85 foam, the maximum velocities are obtained
387 at the inflectional point in the curve showed at Figure 6(b). Regarding the position of the
388 core with respect to velocity peaks, two behaviours are observed in Figure 10. First, the
389 core is located between positive and negative vertical velocity peaks, but always closer
390 to the positive peak. Alongside this, the vertical velocities below the core are generally
391 positive and have an influence on slowing down the core, with the exception of the most
392 permeable k85 foam, where the velocity in the bed located right below the core is
393 negative. The second behaviour detected in the right panel of Figure 10 is that, in contrast
394 with the vertical velocity profiles, the bed horizontal velocity peak is located slightly
395 closer to the axis of symmetry than the core of the primary ring, particularly for the k0
396 solid boundary. This is caused by the no-slip boundary condition present in the solid
397 boundary case, and will be further discussed for the permeable cases by comparing the
398 evolution of the horizontal velocity peaks.
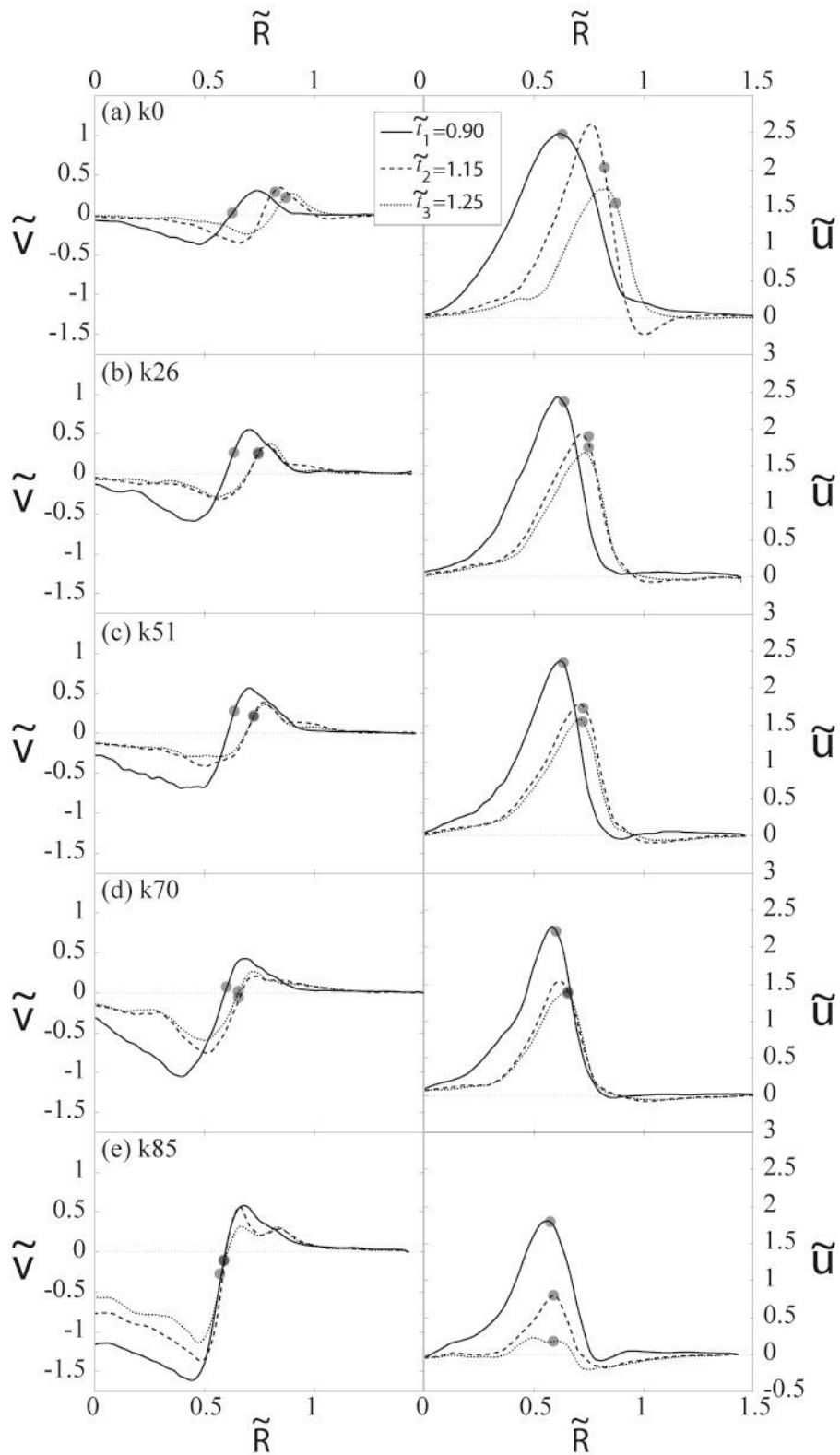
Figure 10. Left column: vertical velocity profiles; right column: horizontal velocity profiles. Results obtained from the PIV velocity fields 1mm above the boundary limit at the same instants as Figure 8. Marks define the position of the centre of the core at each time.

Figure 11 plots the peak horizontal velocity as a function of time, following [19],

specifically

$$\tilde{u}_m(t) = \max_r \tilde{u}(z,r,t), \tag{4}$$

with the criteria of bed velocity defined at a height z = 1mm, used throughout the present article. Bethke and Dalziel [19] found a clear deviation of the solid boundary curve from the inviscid theoretical curve. Moreover, they reported that the same curve for a sediment bed layer did match perfectly with the inviscid plot suggesting that this latter scenario presented a macroscopic free-slip boundary condition (at least in the neighbourhood of the maximum). However, in Figure 11 permeable boundaries do not differ from the solid boundary curve mainly because the measurements are made 1 mm above the bed whereas [19] measured at 0.5mm. Assuming the diffusion of vorticity over a time as D/V_r, then a good approximation to the boundary layer thickness in the k0 case is $\delta \approx (\nu D_t/V_r)^{1/2}$ which yields to a 0.5mm value, suggesting the velocities at $z = 1.0$ mm will be largely uninfluenced by the no-slip condition. The use of $z = 0.5$ mm, which may have provided greater insight into the macroscopic boundary condition, was not feasible due to the nature of the foam.

Table 2. Time occurrence when maximum horizontal bed velocity reaches its peak.

	k0	k26	k51	k70	k85
$\tilde{t}$	1.07	0.96	0.91	0.89	0.85
$\tilde{u}_m(max)$	3.0	2.6	2.4	2.3	2.1
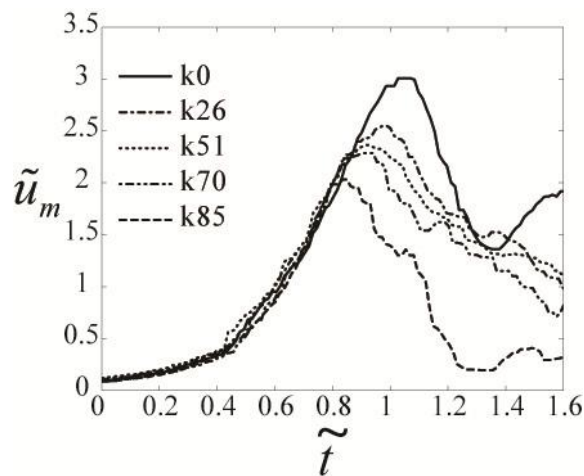
Figure 11. Non dimensional maximum horizontal bed velocity evolution on dimensionless time

423   In Figure 11, time evolution of this maximum horizontal bed velocity is the same for all

424   experiments at early stages of the vortex ring motion. However, after bed velocity for the

425   coarsest boundary, k85, reaches its maximum $\tilde{u}_m$ at $\tilde{t} \approx 0.85$, it decreases and diverges

426   from the general trend of the curve. Similarly, lower permeability boundaries experience

427   the same phenomenon at the times detailed in Table 2. This peak takes place later when

428   permeability decreases –and with higher horizontal velocities– and coincides

429   approximately with the time at which the ring reaches its minimum height and secondary

430   vorticity starts detaching from the boundary. In the k85 case, however, since there is no

431   minimum height, the peak coincides in time at which the slope of the k85 curve in Figure

432   6 (b) changes. The important role played by the permeability differences can also be

433   associated with the existence of fluid exchange between the ambient and the porous

434   boundary. Since the measurements are 2D, the total flux exchanged is computed in the

435   observed area, on the basis that this is representative of all the volume under the

436   assumption of axisymmetry.

437   To calculate fluxes we should use the bed velocity at $z = 0mm$. However, this is not

438   possible experimentally. In a similar calculation, Bethke and Dalziel [19] used the

439   velocities at $z = 0.5mm$ above a bed of particles, but here we were only able to determine

440   reasonable velocities down to $z = 1mm$. Consequently, we shall use the velocity at this

441   height for our calculations.

442   The positive flux, q^+, is defined as the flow coming out of the foam ($v^+ = v$, when $v > 0$)

443   as

$$q^+ (t) = \Delta r \sum_{R_i} v (z_0, r_i, t) r_i \quad \forall r_i, v > 0 . \tag{5}$$

445   Similarly, the negative flux – ambient fluid moving into the porous boundary – is defined

446   using the same terms for negative velocity points ($v^- = v$, when $v < 0$) as,

$$q^- (t) = \Delta r \sum_{r_i} v (z_0, r_i, t) r_i \quad \forall r_i, v < 0 . \tag{6}$$

448   Therefore, the net flux exchanged is the sum of Eq. (5) and Eq. (6),

$$q (t) = q^+ (t) + q^- (t) . \tag{7}$$

450 Assuming there is no flux exchange beyond the limits of the field of view, and that the
451 foam may be considered rigid, we expect no net exchange between the foam and ambient
452 fluid, and thus anticipate $q(t) = 0$.
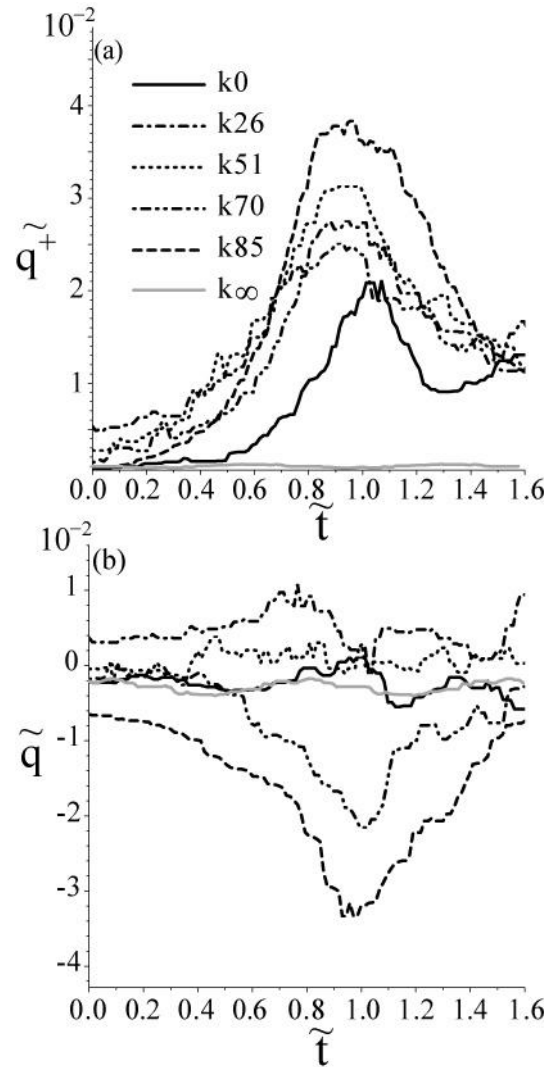
Figure 12. Temporal evolution of the dimensionless flux exchange between the ambient fluid and the boundary. (a) Positive flux from Eq. (5); (b) Total flux exchange.

456 Figure 12 presents the positive and net flux exchange, both in dimensionless form,

457 $\tilde{q} = q \big/ \left(\pi D_t^2 V_r \right)$. Figure 12 (a) shows the positive flux calculated using Eq. (5) and Figure

458 12(b) plots the net flux computed using Eq.(7). The net flux for the solid boundary k0

459 was also computed to determine an estimate of the inherent error in the PIV interrogation

460 process. In general, the net flux computed for the k0 case, Figure 12(b), is negative when

461 the ring is approaching the boundary and starts oscillating. Therefore the dimensionless

462 mean estimative error, using the k0 results of net flux as a reference, is in the order of 10⁻

463 ^{4}, two orders of magnitude below the maximum value of $q^+(t)$ observed for the porous

464 boundaries. The positive flux, $q^+(t)$, in all boundary types is maximum when the primary

465 vortex ring is at its closest approach from the boundary (except for k85 where it occurs

466 when the ring clearly decelerates). However, the peak of the net flux (Figure 12(b)) is

467 slightly retarded with the peak of the positive flux (Figure 12(a)), occurring when the ring

468 diameter is greatest. In Figure 12 (b), two different behaviours are detected: i) for the

469 coarsest foams, k85 and k70, the total flux exchanged is mostly negative, whereas ii) for

470 the finest foams k51 and k26 the total flux is smaller and positive particularly in k26.

471 Predominantly, in Figure 12 conservation of mass (Eq. (7)=0) is not satisfied at any time

472 for any of the experimental measurements with the error always exceeding that for the k0

473 case.

474 There are four candidate mechanisms for the error in $q(t) = 0$: i) the flow exiting the

475 foam is three-dimensional with azimuthal variations not captured by the current methods;

476 ii) the relatively slow camera shutter speed means slower particles create brighter images

477 near the bottom and the PIV may be biased towards them; iii) the foam filters some of the

478 particles from the flow so that there are many fewer particles in the upward flow

479 (contributing to q^+) creating a bias in the measurements; and iv) the limited resolution of

480 the PIV processing that effectively smooths any localised fast-moving jets issuing from

481 the individual pores. The first of these possibilities affects mainly the coarser foams due

482 to higher velocities and larger pore diameter, introducing a larger 3D effect. The second

483 candidate might explain the effects found on the solid boundary and the finer foams,

484 where net flux is positive during all the experiment. The third candidate affects mainly

485 coarser foams because incoming velocities (which are higher in the most permeable

486 boundaries) make the particles lying at the surface of the foam be exhausted sooner.

487 Moreover, this fluid may have been in the foam for a while and so is likely to have

488 deposited its particles. Finally, the fourth candidate affects all foams independently.

489 Assuming the third error type is the dominant effect, positive flux is corrected by

490 modifying positive velocities coming out of the foam at a height $z = 1$ mm.

491 **4   Discussion**

492 The experiments on the impact with a solid wall, reported in the last section, confirm the

493 observation by previous researchers that the interaction goes through three phases,

494 namely: i) stretching due to the presence of its mirror image in the boundary, ii) the

495 generation of secondary vorticity of the opposite sign that forms a secondary ring that iii)

496 drives a rebound of the primary ring from the wall and causes the trajectory of the cores

497 to loop. When permeable boundaries are used, all three of these phenomena are reduced

498 as permeability increases. In particular, in the most permeable foam, k85, the ring does

499 not rebound but continues to propagate forwards and dissipates. This is confirmed by

500 looking at the flux of primary vorticity across $z = 1\,\mathrm{mm}$ computed as

501
$$q_{\omega} = \Delta r \sum_{R_i} \omega\left(z, r_i, t\right) v_i\left(z, r_i, t\right) r_i \quad \omega > 0.03\,\omega_{\max} \,, \tag{8}$$

502 and made dimensionless by $\tilde{q}_{\omega} = q_{\omega} / \left(D_t V_r^2\right)$. The results obtained for the k85 case are

503 shown in Figure 13 where a clear change is visible after $\tilde{t} > \tilde{t}_1$, which is right after the

504 frame at which the primary vorticity starts decreasing in Figure 9(a). This also explains

505 why the primary vorticity in the k85 permeable boundary decreases faster than the other

506 boundary types: because the primary ring seems to enter inside the foam. This does not

507 occur with the other cases as seen in Figure 8. Comparing the results with the k0 case,

508 and bearing in mind that secondary vorticity in the k85 case is weaker, most of the

509 decrease in vorticity shown in Figure 9 is due to the vortex ring penetrating/dissipating

510 the foam. However it is not clear which fraction of the circulation disappears through the

511 porous boundary and this question is left for future investigations.
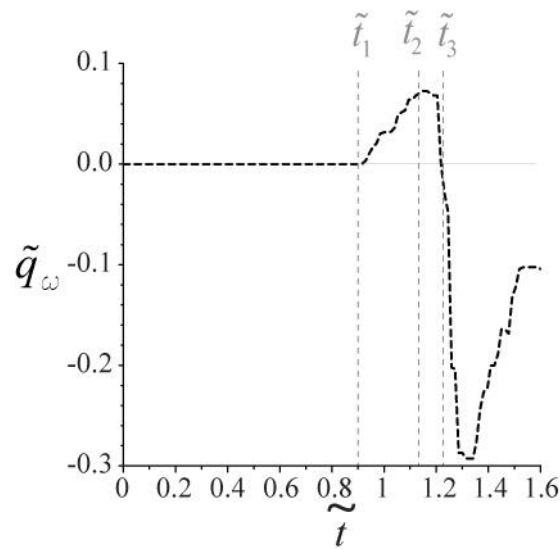
512

513 **Figure 13. Flux of primary vorticity through the k85 porous media, measured at *z=1mm*.**

514 The permeable boundary results shown in this study are contrasted with two similar

515 situations: bed sediments and thin porous grids. When comparing two different sediment

516 bed layers (with different particle diameter and permeability), Bethke and Dalziel [19]

517 found that the trajectory followed by the vortex ring core was not noticeably affected by

518 the bed permeability, although they report a weak exchange with the bed and an

519 enhancement in the velocity immediately above the bed. The first of these observations

520 contrasts with what we see here in Figure 6. The principal reason behind this difference

521 is that the permeability of their porous media ($\kappa < 9.4 \times 10^{-10}$ m^2) was between two and

522 four orders of magnitude smaller than for the foams presented here, and consequently the

523 flow into and out of the porous media was very much smaller and so had no measureable

524 impact on the propagation of the ring. Also, our present results suggest the difference in

525 approach distance would not have been measurable for such low permeabilities. To a

526 good approximation, their porous boundaries were indistinguishable from solid

527 boundaries except for the dynamics of the boundary layer that formed on it. However,

528 with the substantially larger permeabilities used here, we see that the permeability has a

529 clear influence on the vortex ring diameter expansion, the rebound and the minimum

530 height reached close to the boundary.

531 The evolution of the ring approaching boundaries with relatively high permeability is

532 very similar to that of a vortex ring impinging on a thin porous grid (e.g.[20], [21], and

533 [22]). Experimental setups differ with the research presented herein essentially at the

534 position of the boundary and its thickness: they used very thin grids located far from the

535 solid boundary, and the grid did not cover the entire plan form of the tank. Moreover, as

536 with the porous grids, the pressure drop across the grid could be altered by changing either

537 the porosity, or the size of the wires. Therefore the flux beyond the limit of the porous

538 grids is substantially different from the flux inside thicker porous boundaries as the ones

539 used in our experiments. However it is worth to compare experiments because, to a good

540 approximation, all our foams have the same porosity.

541 In the wire grid experiments, the decrease in vortex stretching and the changes in

542 secondary vorticity formation are explained to be due to the loss of circulation of the

543 primary ring, a feature also seen in Figure 9. According to Adhikari and Lim [20], this is

544 caused by the self-induced flow around the axis of symmetry that forms a jet-like flow

545 beyond the grid. In Naaktgeboren et al. [21] the decrease in the impulse with more porous

546 grids, as a reflection of the drag force exerted on the flow by the grids, was said to cause

547 the reduction of the secondary vorticity and subsequent rebound. However, neither of

548 these investigations take into account either the penetration of the boundary layer inside

549 the porous media or the flux exchange between the downstream and upstream sides of the

550 grid.

551 Recalling that one of the main differences between our experiments and the thin grid

552 research already published is that the latter does not cover the whole plan form of the

553 tank, the flux exchange between both sides of the grid is clearly influenced by this. From

554 Figure 10, peak vertical velocities detected at the boundary increases with permeability.

555 Therefore the velocity coming out of the foam is higher in the coarsest case, k85,

556 constraining the diameter of the ring and preventing the stretching. Combining both

557 results, the reduced stretching when permeability increases is due to the smaller decrease

558 in the flow near the axis of symmetry and the subsequent increase in flux exiting of the

559 foam.

560 The macroscopic no-slip condition, satisfied in the solid boundary scenario and linked to

561 the formation of the secondary vorticity, is found to disappear as permeability increases.

562 This is consistent with the results from [21] that relate the suppression of the secondary

563 vorticity to the decrease in hydraulic impulse with grids of higher permeability. Bethke

564 and Dalziel [19] suggested the explanation for the apparent slip condition at the surface

565 of a 1000 μm bed sediment layer was, partly, the permeability of the layer itself. Although

566 there is no pattern visible from the evolution of the secondary vorticity with permeability

567 in Figure 9b, the decrease in primary circulation as permeability increases shows how the

568 no-slip boundary condition will also be affected by permeability.

569 Another phenomenon associated with different permeable beds is related to the boundary

570 layer formed at the interface. As has already been noticed in the previous section and

571 according to [19], the maximum velocity just above the bed for a ring impinging a

572 sediment bed layer evolves in the same way as for an inviscid vortex ring. Nevertheless,

573 slow moving fluid that can be equated with a boundary layer is still present, as witnessed

574 by what looks like the boundary layer separation that occurs even when the k85 foam is

575 used. However, the detachment of this layer with the consequent formation of the

576 secondary vortex ring differs from one boundary type to the other. As suggested by Figure

577 11, the maximum of the peak velocity just above the bed is reached earlier for higher k

578 values and coincides with the detachment of the boundary layer and the formation of the

secondary vortex ring. The coherence of this secondary vortex, formed right after the ring reaches its minimum height, is lost due to two factors: the flux exchange and the extension of the boundary layer into the porous material found by Beavers and Joseph [25]. When a more permeable boundary is used, the boundary layer is thicker and so higher stresses are needed to permit the entire detachment. This, added to the fact that the k85 boundary has a lower maximum bed velocity peak compared to less permeable boundary types, explains the poor coherence of the secondary vortex ring formed while approaching a high permeable boundary, as shown in Figure 8.

5   Conclusions

The experiments reported here explored the interaction of vortex rings with different permeable boundaries. Vortex rings impinging a solid boundary were also studied in order to compare the main characteristics of their motion towards the boundary with the permeable cases.

The foams used had a finite thickness of 25 mm, except the coarsest k85 foam that was 50 mm thick. However, over this range, no influence of h was found in the experiments, suggesting that the results presented herein can be extended to thicker permeable boundaries.

Results obtained using PIV showed how permeability affects the characteristics already found for vortex rings moving towards a solid boundary. Permeable boundaries changed:

a) The diameter stretching: as permeability increases, the diameter of the primary ring is stretched less.

b) The primary ring deceleration: the influence of the boundary decreases as permeability increases.

c) The secondary vortex ring formation: higher permeable boundaries presented a less coherent secondary ring with shorter life. This affects the negative stretching and the rebound of the primary ring. Moreover, the secondary vortex ring was formed earlier for higher permeable boundaries, mainly because primary vortex ring reached the interface faster.

607 The analysis of velocities close to the boundary in an attempt to quantify the fluxes
608 between the free fluid and the porous layer, and the velocities within any boundary layer,
609 revealed a significant influence of the height above the interface at which the
610 measurements were taken. Unfortunately, we were unable to complete these
611 measurements closer than 1 mm above the boundary due to the characteristics of the foam.
612 While this was sufficiently close to analyse the vertical velocities, the analysis of the no-
613 slip/slip boundary condition at the interface was more complicated. Maximum radial
614 velocity results were less strongly affected by the no-slip boundary condition on the solid
615 boundary than the experiment performed by [19] Z at which it is measured. Moreover,
616 when secondary vorticity was computed, other errors regarding the choice of the interface
617 level ($\tilde{z} = 0$) proved to be important as well.

618 The radial velocity analysis showed an apparent evolution of the peak horizontal velocity
619 from that associated with a no-slip boundary condition for a solid boundary to that of a
620 slip boundary condition for permeable boundaries, despite the limitations imposed by the
621 measurement height. This was confirmed with the previous analysis of the primary
622 circulation evolution. This is broadly consistent with the suggestion by [19] for a particle
623 layer.

624 Four of the five cases studied showed similar phases in the evolution of a vortex ring
625 whether the boundary was solid or permeable. The exception to this was for the coarsest
626 foam, k85, where the ring penetrated the foam. However, the vertical structure of the ring
627 did not survive within the porous layer.

628 Finally, the research presented herein has shown that further investigation is needed for
629 the interactions of vortex rings with permeable boundaries. For instance, azimuthal
630 variations of the vortex ring characteristics were omitted from the analysis presented so
631 far. Moreover, additional experiments are needed using different Reynolds numbers to
632 see its influence on permeable boundaries and to determine the key dimensionless
633 grouping that characterises the interaction.

6 Acknowledgements

7   References

641 [1]   M. Staymates and G. Settles, "Vortex ring impingement and particle suspension,"
642   *Bull. Am. Phys. Soc.*, 2005.

643 [2]   W. Stewart, "Helicopter Behaviour in the Vortex-Ring Conditions," *Aeronaut.*
644   *Res. Committee, R&M*, no. 3117, 1951.

645 [3]   S. Newman, R. Brown, J. Perry, S. Lewis, M. Orchard, and A. Modha,
646   "Comparative numerical and experimental investigations of the vortex ring
647   phenomenon in rotorcraft," *Am. Helicopter Soc. Int.*, 2001.

648 [4]   Lord Kelvin, "The translatory velocity of a circular vortex ring," *Phil. Mag.*, vol.
649   33, pp. 511–512, 1867.

650 [5]   M. J. M. Hill, "On a Spherical Vortex.," *Proc. R. Soc. London*, vol. 55, no. 331–
651   335, pp. 219–224, 1894.

652 [6]   G. K. Batchelor, *An introduction to fluid dynamics*. Cambridge University Press,
653   UK, 1967.

654 [7]   J. Norbury, "A family of steady vortex rings," *J. Fluid Mech.*, vol. 57, pp. 417–
655   431, 1973.

656 [8]   T. Maxworthy, "Some experimental studies of vortex rings," *J. Fluid Mech.*, vol.
657   81, pp. 465–495, 1977.

658 [9]   P. G. Saffman, "The approach of a vortex pair to a plane surface in inviscid
659   fluid," *J. Fluid Mech.*, vol. 92, pp. 497–503, 1979.

660 [10] J. Cerra A. W. and C. R. Smith, "Experimental observations of vortex ring
661   interaction with the fluid adjacent to a surface," *Interim Rep. Lehigh Univ.,*
662   *Bethlehem, PA. Dept. Mech. Eng. Mech.*, vol. 1, 1983.

663 [11] J. D. A. Walker, C. R. Smith, A. W. Cerra, and T. L. Doligalski, "The impact of a
664   vortex ring on a wall," *J. Fluid Mech.*, vol. 181, pp. 99–140, 1987.

665 [12] P. Orlandi and R. Verzicco, "Vortex rings impinging on walls: axisymmetric and
666   three-dimensional simulations," *J. Fluid Mech.*, vol. 256, p. 615, 1993.

667 [13] J. D. Swearingen, J. D. Crouch, and R. A. Handler, "Dynamics and stability of a
668   vortex ring impacting a solid boundary," *J. Fluid Mech.*, vol. 297, pp. 1–28,
669   1995.

670 [14] T. T. Lim, T. B. Nickels, and M. S. Chong, "A note on the cause of rebound in
671   the head-on collision of a vortex ring with a wall," *Exp. Fluids*, vol. 12, no. 1, pp.
672   41–48, 1991.

673 [15] R. J. Munro and S. B. Dalziel, "Attenuation technique for measuring sediment
674   displacement levels," *Exp. Fluids*, vol. 39, pp. 602–613, 2005.

675 [16] N. Bethke, "Vortex Ring Interaction with a Particle Layer: Implications for
676   Sediment Transport," PhD Thesis. Department of Applied Mathematics and
677   Theoretical Physics, University of Cambridge, 2008.

678 [17] R. J. Munro, N. Bethke, and S. B. Dalziel, "Sediment resuspension and erosion
679   by vortex rings," *Phys. Fluids*, vol. 21, p. 046601, 2009.

680 [18] N. Masuda, J. Yoshida, B. Ito, T. Furuya, and O. Sano, "Collision of a vortex
681   ring on granular material. Part I. Interaction of the vortex ring with the granular
682   layer," *Fluid Dyn. Res.*, vol. 44, no. 1, p. 15501, 2012.

683 [19] N. Bethke and S. B. Dalziel, "Resuspension onset and crater erosion by a vortex
684   ring interacting with a particle layer," *Phys. Fluids*, vol. 24, no. 6, p. 063301,
685   2012.

686 [20] D. Adhikari and T. T. Lim, "The impact of a vortex ring on a porous screen,"
687   *Fluid Dyn. Res.*, vol. 41, no. 5, p. 051404, Oct. 2009.

688 [21] C. Naaktgeboren, P. S. Krueger, and J. L. Lage, "Interaction of a laminar vortex
689   ring with a thin permeable screen," *J. Fluid Mech.*, vol. 707, pp. 260–286, Jul.
690   2012.

691 [22] J. T. Hrynuk, J. Van Luipen, and D. Bohl, "Flow visualization of a vortex ring
692   interaction with porous surfaces," *Phys. Fluids*, vol. 24, p. 37103, 2012.

693 [23] S. B. Dalziel, "DigiFlow User Manual." 2006.

694 [24] S. E. Widnall, D. B. Bliss, and C. Y. Tsai, "The instability of short waves on a
695   vortex ring," *J. Fluid Mech.*, vol. 66, no. 1, pp. 35–47, 1974.

696 [25] G. S. Beavers and D. D. Joseph, "Boundary conditions at a naturally permeable
697   wall," *J. Fluid Mech*, vol. 30, no. 1, pp. 197–207, 1967.

698 [26] G. I. Taylor, "A model for the boundary condition of a porous material. Part 1,"
699   *J. Fluid Mech.*, vol. 49, no. 02, p. 319, Mar. 1971.

700 [27] S. Richardson, "A model for the boundary condition of a porous material. Part
701   2," *J. Fluid Mech*, vol. 49, no. 2, pp. 327–336, 1971.

702